Electronic Supplementary Information (ESI) for

Interlayer spacing in pillared and grafted MCM-22 type silicas: Density functional theory analysis versus experiment

Yong Han,*[a,b] Puranjan Chatterjee,[a,c] Sardar B. Alam,[a] Tanya Prozorov,[a] Igor I. Slowing[a,c] and James W. Evans[a,b]

[a] Division of Chemical and Biological Sciences, Ames National Laboratory, Ames, Iowa 50011, USA
[b] Department of Physics and Astronomy, Iowa State University, Ames, Iowa 50011, USA
[c] Department of Chemistry, Iowa State University, Ames, Iowa 50011, USA

*Corresponding author email: y27h@ameslab.gov

Contents

ESI1. Effect of Al content on interlayer spacing in MCM-22 materials

ESI2. Effect of pillaring agent on interlayer spacing in MCM-22 materials

ESI3. DFT benchmark analysis for bulk property of a-quartz

ESI4. DFT benchmark analysis for the geometric structures of trimethylsilanol and propane

ESI5. DFT benchmark analysis for bulk property of MCM-22 with Si:Al = 1:0

ESI6. Synthesis and XRD and FTIR analysis of pillared MCM-22

ESI7. Analysis of interlayer spacings in MCM-22 and AP-MCM-22 from STEM

ESI8. MD simulation parameters with empirical ReaxFF

**ESI9. Characterization of different classes of H-bonding**

ESI10. Atomic spacings between H atoms and their surrounding atoms

ESI11. Relative thermodynamic stability of pillared versus grafted configurations

ESI1. Effect of Al content on interlayer spacing in MCM-22 materials

Here, we assess the dependence of interlayer spacing in MCM-22 materials on the Al content specifically by examining and comparing materials for Si:Al = 51:1, 42:1, and 20:1. The goal of this analysis is to provide support for our claim that there should be no significant difference between this spacing for materials with Si:Al = 51:1 and for pure silica MCM-22. This analysis utilizes x-ray diffraction (XRD), as described in Section 2.2 for the analysis of MCM-22P, MCM-22 with Si:Al = 51:1, and MCM-22 with Si:Al = 51:1 after exposure to pillaring agent. The Si:Al = 51:1 ratio implies only slightly more than one substituted Al per unit cell of pure silica version of MCM-22 (which has 72 Si). Even with a potential preference for Al to substitute a Si at the surface of MCM-22 layers [26], we suggested that such substitution should have negligible effect on interlayer spacing.

This hypothesis is supported by the fact that the reported interlayer *d*-spacing in ITQ-1 (pure silica analogue of MCM-22) is ca. 25 Å [22] which is similar to the *d*-spacing of our MCM-22. To assess the Al amount needed in the material to obtain noticeable changes in the *d*-spacing, we prepared two more MCM-22 materials with Si:Al ratios of 42:1 and 20:1, which correspond to ca. 1.7 and 3.4 Al atoms per unit cell, respectively. Prior to calcination, both materials showed similar *d*-spacing (ca. 27 Å) as in that of our original material (with Si:Al = 51:1). While the material with Si:Al = 42:1 ratio, i.e., 42:1 MCM-22, showed similar *d*-spacing (ca. 25.4 Å) to that of 51:1 MCM-22 (ca. 25.3 Å), the 20:1 MCM-22 exhibited a significantly larger *d*-spacing of ca. 26.5 Å. See **Fig. S1**. Therefore, we can conclude that only MCM-22 materials with Si:Al ratio below about 40:1 show noticeably different interlayer spacing than pure silica MCM-22.
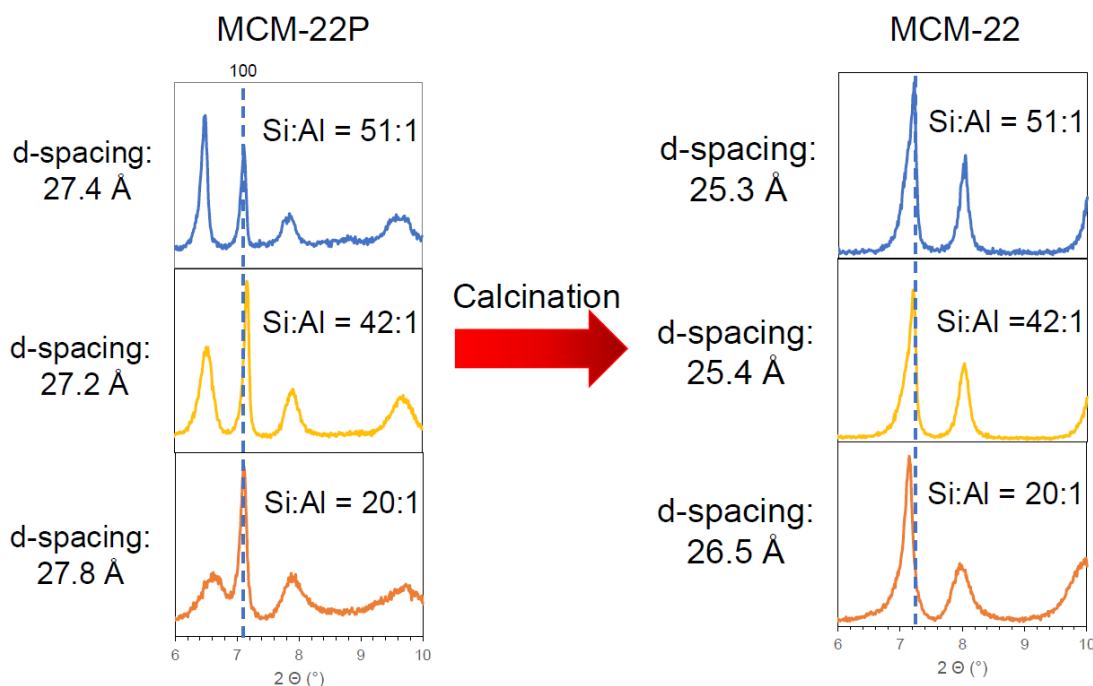
Fig. S1. Powder XRD data for MCM-22P and for MCM-22 with three different Al contents.

ESI2. Effect of pillaring agent on interlayer spacing in MCM-22 materials

Here, we assess the dependence of interlayer spacing in pillared MCM-22 materials on the molecular composition of the pillaring agent, and specifically on the length of the hydrocarbon chain. We suggested that the chain should lie roughly parallel to the layers in MCM-22, and thus its length should not have a significant impact on interlayer spacing. We utilize the DFT methodology described in Section 2.1, and follow the procedure described in Section 3.2 for studies of partial pillaring of MCM-22 with 50% −OH + 50% (−O$_2$)SiOHCH$_3$ (i.e., half of the −OH pairs on adjacent surfaces in an interlayer space are replaced by pillars of the form (−O$_2$)SiOHCH$_3$ where the −O$_2$ in this unit come from the two O in an −OH pair). Now instead we perform an analysis where the (−O$_2$)SiOHCH$_3$ pillar is replaced by (−O$_2$)SiOHCH$_2$CH$_3$. Results are shown in **Fig. S2** for the variation of system energy with interlayer spacing for partially pillared MCM-22 comparing results for (−O$_2$)SiOHCH$_2$CH$_3$ and (−O$_2$)SiOHCH$_3$ pillars. From the minima in these curves, it follows that the difference in interlayer spacing for these two types of pillars is only 0.2 Å. This result supports the above claim.
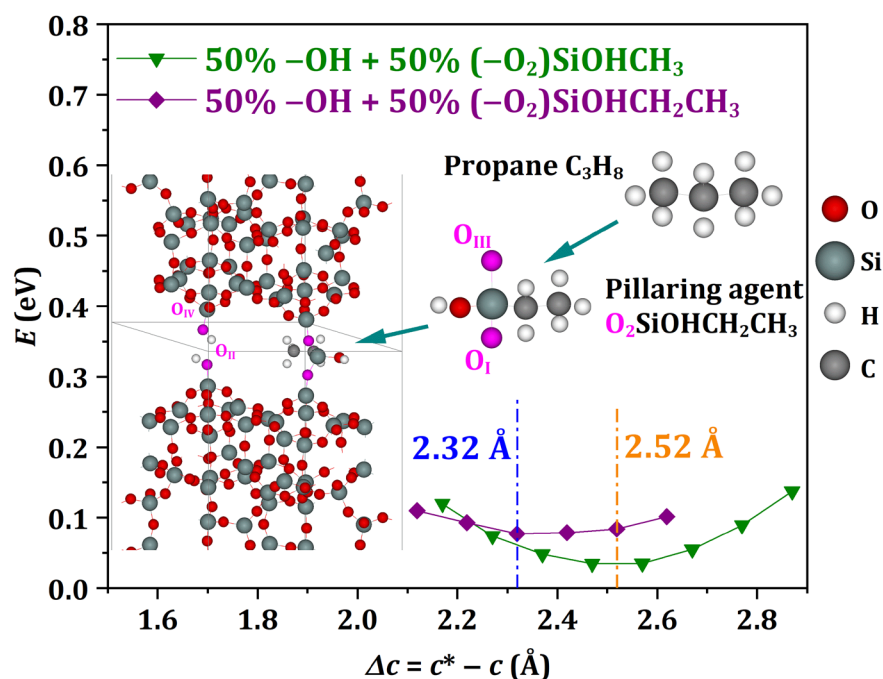

Fig. S2. System energy versus interlayer spacing for partially pillared MCM-22 comparing results for (−O$_2$)SiOHCH$_2$CH$_3$ pillars (purple curve) and (−O$_2$)SiOHCH$_3$ pillars (green curve, the same as the green curve in **Fig. 3b**).

For the above analysis with (−O$_2$)SiOHCH$_2$CH$_3$ pillars, the initial geometry of the chain in the DFT calculation was selected guided by the geometry of propane (but replacing one C by Si, etc., as indicated by the insets in **Fig. S2**). Of course, the initial orientation of the geometry is not critical (as discussed for **Fig. 3b**), and relaxation of atomic coordinates is

performed before reporting system energies. However, it is instructive to assess how well the DFT functional utilized in this analysis recovers the geometry of propane. This is provided in **Section ESI4**.

ESI3. DFT benchmark analysis for bulk property of α-quartz

In order to assess the effectiveness of the optB88-vdW functional for silica systems, we first calculate the bulk properties of a typical silica polymorph, α-quartz, for which the experimental data of bulk property are available for the purpose of comparison with our DFT results. The α-quartz crystal has a hexagonal structure, and the unit cell contains three Si atoms and six O atoms (the unit cell formula is denoted as Si_3O_6), as illustrated in **Fig. S3.** In our DFT calculations for α-quartz, the supercell is taken to be the unit cell with a k mesh of $50 \times 50 \times 50$. As listed in **Table S1**, the lattice constants a and c, the bulk modulus B_0, the first derivative B_0' of the bulk modulus with respect to pressure, and the formation enthalpy ΔH_f from our optB88-vdW calculations are in excellent agreements with experimental values. As a comparison, we also use the most common PBE GGA functional and the obtained bulk properties are still reasonably good but overall, slightly worse in contrast to the results from the optB88-vdW functional (see **Table S1**).

(a)　　　　　　　**(b)**
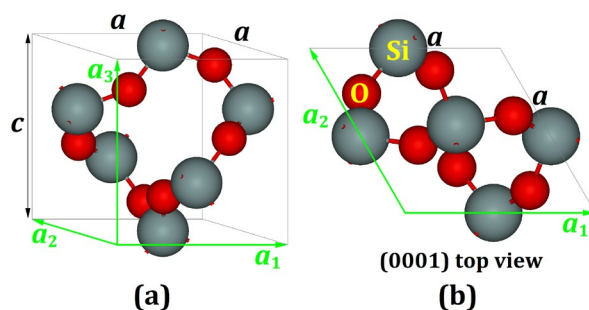
Fig. S3. (a) A 3D view and (b) a (0001) top view of α-quartz. Three primitive vectors $\boldsymbol{a_1}$, $\boldsymbol{a_2}$, and $\boldsymbol{a_3}$ of the hexagonal unit cell (Si_3O_6) are indicated with $|\boldsymbol{a_1}| = |\boldsymbol{a_2}| = a$, $|\boldsymbol{a_3}| = c$, $\alpha = \beta = 90°$, and $\gamma = 120°$, where α, β, and γ are the angles between $\boldsymbol{a_2}$ and $\boldsymbol{a_3}$, between $\boldsymbol{a_1}$ and $\boldsymbol{a_3}$, and between $\boldsymbol{a_1}$ and $\boldsymbol{a_2}$, respectively.

In the above calculations for lattice constants, we always fully relax the coordinates of all atoms in the unit cell as well as the cell volume and shape for obtaining a configuration with energy E_0 and corresponding volume V_0. To obtain the elastic properties, we relax the cell shape for a series of configurations with volumes fixed around V_0 to ensure the global energy minimum E_0. Then, we use the Stacey-Vinet equation of state [49, 50],

$$E = E_0 + \frac{2V_0 B_0}{(B_0' - 1)^2}\left(2 - \left\{5 + 3B_0'\left[\left(\frac{V}{V_0}\right)^{\frac{1}{3}} - 1\right] - 3\left(\frac{V}{V_0}\right)^{\frac{1}{3}}\right\}e^{\frac{3}{2}(B_0'-1)\left[1-\left(\frac{V}{V_0}\right)^{\frac{1}{3}}\right]}\right), \quad (S1)$$

to fit the data points of energy E versus volume V so that B_0 and B_0' are attained. The formation enthalpy ΔH_f at 0 K [51] is obtained from

$$\Delta H_\mathrm{f} = \frac{E_{(\mathrm{SiO_2})_n}}{n} - E_\mathrm{Si} - E_{\mathrm{O_2}}, \tag{S2}$$

where $E_{(\mathrm{SiO_2})_n}$ is the unit cell total energy of a silica polymorph ($n = 3$ and 72 for α-quartz and ITQ-1, respectively), E_Si is the energy per Si atom in the bulk Si crystal with diamond structure, and $E_{\mathrm{O_2}}$ is the energy of a molecule O_2 in gas phase.

Table S1. Bulk property of α-quartz, predicted from our DFT calculations and compared with available experimental values. a or c is the lattice constant. B_0 and B_0' are obtained from Eq. (S1) for the bulk modulus and the first derivative of the bulk modulus with respect to pressure, respectively. The formation enthalpy ΔH_f at 0 K is obtained from Eq. (S2).

Method	a (Å)	c (Å)	B_0 (GPa)	B_0'	ΔH_f (eV)
DFT, PBE GGA	5.0409	5.5281	30.82	5.1	−8.431
DFT, optB88-vdW	4.9168	5.4298	39.98	4.5	−9.004
Experiments	4.916(1)[a]	5.4054(4)[a]			
	4.9021(1)[b]	5.3997(1)[b]			
	4.914(1)[c]	5.406(1)[c]	38.979[d]	5.8[d]	
			37.405[e]	6.3[e]	−9.516[f]

[a]At 1 atm [52].
[b]At 13 K [53].
[c]At 1 bar [54].
[d]At −195.8 °C [55].
[e]At 25 °C [55].
[f]At 0 K [56].

ESI4. DFT benchmark analysis for the geometric structures of trimethylsilanol and propane

Trimethylsilanol is an organosilicon compound with the chemical formula $C_3H_{10}OSi$ or $(CH_3)_3SiOH$. A trimethylsilanol molecule contains one centered Si atom with three methyl groups CH_3 and one hydroxyl group OH. The optimized geometry of one trimethylsilanol molecule in a rectangular supercell of 24.3 Å × 24.2 Å × 24.1 Å with a k mesh of $1 \times 1 \times 1$ from our optB88-vdW calculation is shown on the left of **Fig. 4a or 5a**. The Cartesian coordinates x, y, and z of 15 atoms in the molecule are listed in **Table S2** from our PBE and optB88-vdW calculations. From these coordinates, any atomic spacings s (as used in **Section ESI10**), bond lengths, and bond angles can be readily obtained. In addition, we also obtain the formation enthalpies $\Delta H_\mathrm{f} = -6.130$ and -5.271 eV at 0 K for one trimethylsilanol molecule from our PBE and optB88-vdW calculations, respectively, by using

$$\Delta H_\mathrm{f} = E_{\mathrm{C_3H_{10}OSi}} - 3E_\mathrm{C} - 5E_{\mathrm{H_2}} - \frac{E_{\mathrm{O_2}}}{2} - E_\mathrm{Si}, \tag{S3}$$

where $E_{C_3H_{10}OSi}$ is the total energy of a trimethylsilanol molecule, E_C is the energy per C atom in bulk graphite, E_{Si} is the energy per Si atom in the bulk Si crystal with diamond structure, E_{H_2} is the energy of a molecule H_2 in gas phase, and E_{O_2} is the energy of a molecule O_2 in gas phase.

Table S2. The Cartesian coordinates x, y, and z (in Å) of 15 atoms in an optimized trimethylsilanol molecule from our PBE and optB88-vdW calculations. A number in the first column denotes the ID of an elemental atom.

	PBE			optB88-vdW		
Atoms	x	y	z	x	y	z
C1	11.78260	9.85026	9.39315	11.77890	9.85075	9.39300
C2	8.97876	8.55630	9.43684	8.97964	8.55787	9.43671
C3	9.26504	11.63102	9.39328	9.26651	11.62786	9.39334
O4	9.95386	9.93529	11.67627	9.95820	9.93790	11.67160
Si5	10.00908	10.01297	10.00164	10.00865	10.01240	9.99936
H6	12.23269	8.91326	9.75203	12.22964	8.91589	9.75187
H7	11.82515	9.84311	8.29340	11.82270	9.84430	8.29493
H8	12.41490	10.68101	9.74070	12.40824	10.68128	9.74168
H9	8.94051	8.50259	8.33909	8.94040	8.50304	8.34040
H10	9.39821	7.61043	9.80786	9.39825	7.61333	9.80758
H11	7.94731	8.63701	9.80813	7.94975	8.63792	9.80798
H12	8.23175	11.74309	9.75257	8.23495	11.74152	9.75224
H13	9.83782	12.50380	9.74095	9.84017	12.49786	9.74180
H14	9.24384	11.66882	8.29357	9.24578	11.66689	8.29524
H15	10.43349	10.61254	12.17582	10.43322	10.61271	12.17758

Table S3. The Cartesian coordinates x, y, and z (in Å) of 11 atoms in an optimized propane molecule from our PBE and optB88-vdW calculations. A number in the first column denotes the ID of an elemental atom.

	PBE			optB88-vdW		
Atoms	x	y	z	x	y	z
C1	10.00003	9.43225	10.00001	10.00003	9.43135	10.00003
C2	8.72692	10.27917	9.99995	8.72695	10.27998	9.99993
C3	11.27310	10.27928	10.00015	11.27314	10.28007	10.00017
H4	9.99995	8.76842	10.87982	9.99988	8.77029	10.87925
H5	10.00010	8.76858	9.12005	10.00008	8.77050	9.12062
H6	8.68491	10.92961	10.88679	8.68614	10.92826	10.88569
H7	8.68507	10.92961	9.11308	8.68628	10.92815	9.11403
H8	7.82180	9.65541	9.99982	7.82467	9.65600	9.99992
H9	12.17822	9.65554	10.00010	12.17540	9.65611	10.00023
H10	11.31494	10.92975	10.88697	11.31366	10.92838	10.88591
H11	11.31497	10.92968	9.11325	11.31376	10.92821	9.11423

Propane has the molecular formula C_3H_8, which is a three-carbon alkane. The optimized geometry of one propane molecule in a rectangular supercell of 24.3 Å × 24.2 Å × 24.1 Å with a k mesh of 1 × 1 × 1 from our optB88-vdW calculation is shown as an inset in **Fig. S2**. The Cartesian coordinates x, y, and z of the 11 atoms in the molecule are listed in **Table S3** from our PBE and optB88-vdW calculations. From these coordinates, any

atomic spacings s, bond lengths, and bond angles can be readily obtained. In addition, we also obtain the formation enthalpies $\Delta H_f = -2.274$ and -1.509 eV at 0 K for one propane molecule from our PBE and optB88-vdW calculations, respectively, by using

$$\Delta H_f = E_{C_3H_8} - 3E_C - 4E_{H_2}, \tag{S4}$$

where $E_{C_3H_8}$ is the total energy of a propane molecule, E_C is the energy per C atom in bulk graphite, and E_{H_2} is the energy of a molecule H_2 in gas phase.

ESI5. DFT benchmark analysis for bulk property of MCM-22 with Si:Al = 1:0

In order to assess the effectiveness of the optB88-vdW functional, we assess the bulk property of ITQ-1 (i.e., MCM-22 with Si:Al = 1:0) with a unit cell formula of $Si_{72}O_{144}$ (see **Fig. 1a-c**). The lattice constants a and c from our optB88-vdW calculations are in good agreements with experimental values and better than the results from PBE functional, as listed in **Table S4**. We also predict B_0, B_0', and ΔH_f from our optB88-vdW and PBE calculations, using Eqs. (S1) and (S2), respectively. The experimental values of B_0, B_0', and ΔH_f are unavailable in literature and therefore the experimental measurements for these quantities are suggested. We also noticed that our PBE calculations predict a negative $B_0' = -0.9$, which might be not reasonable physically, although the fitted B_0' value is generally not very sensitive to the data points on the energy-volume curve Eq. (S1). In contrast, $B_0' = 3.5$ from our optB88-vdW functional is expected to be a reasonable value.

Table S4. Bulk property of ITQ-1 (i.e., MCM-22 with Si:Al = 1:0), predicted from our DFT calculations and compared with available experimental values. a or c is the lattice constant. B_0 and B_0' are obtained from Eq. (S1) for the bulk modulus and the first derivative of the bulk modulus with respect to pressure, respectively. The formation enthalpy ΔH_f at 0 K is obtained from Eq. (S2). As a comparison, the lattice constants of MCM-22 with composition $H_{2.376}Na_{3.096}(Al_{0.360}B_{5.112}Si_{66.528})O_{144}$ from early experiments are also listed.

| Crystal	Method	a (Å)	c (Å)	B_0 (GPa)	B_0'	ΔH_f (eV)
ITQ-1, unit cell formula: $Si_{72}O_{144}$						
	DFT, PBE GGA	14.4811	25.3607	62.67	-0.9	-8.416
	DFT, optB88-vdW	14.4542	25.2094	61.56	3.5	-8.839
	Experiments	14.2081(1)[a]	24.945(2)[a]			
		14.1827(1)[b]	25.007(3)[b]			
MCM-22, unit cell formula: $H_{2.376}Na_{3.096}(Al_{0.360}B_{5.112}Si_{66.528})O_{144}$						
	Experiment	14.1145(8)[c]	24.8822(18)[c]			

[a]Ref. [22].
[b]Ref. [57].
[c]Ref. [14].

For the purpose as a k-point test, in the above bulk calculations for ITQ-1, we intentionally use a larger k mesh of $12 \times 12 \times 6$. To ensure a sufficiently large k mesh in the calculations with agents, we use the PBE functional obtaining the unit cell total energies 24.75, -0.72, -0.30, -0.15, -0.04, and 0.04 meV for the k meshes of $1 \times 1 \times 1$, $2 \times 2 \times 1$,

$4 \times 4 \times 2$, $6 \times 6 \times 3$, $8 \times 8 \times 4$, and $10 \times 10 \times 5$, relative to the energy for the k mesh of $12 \times 12 \times 6$, respectively. This indicates that the k mesh of $1 \times 1 \times 1$ is not sufficiently large, while the total energy for the k mesh of $2 \times 2 \times 1$ has been well converged and therefore we take the k mesh of $2 \times 2 \times 1$ in all DFT calculations in **Sections 3, 4, and 5**.
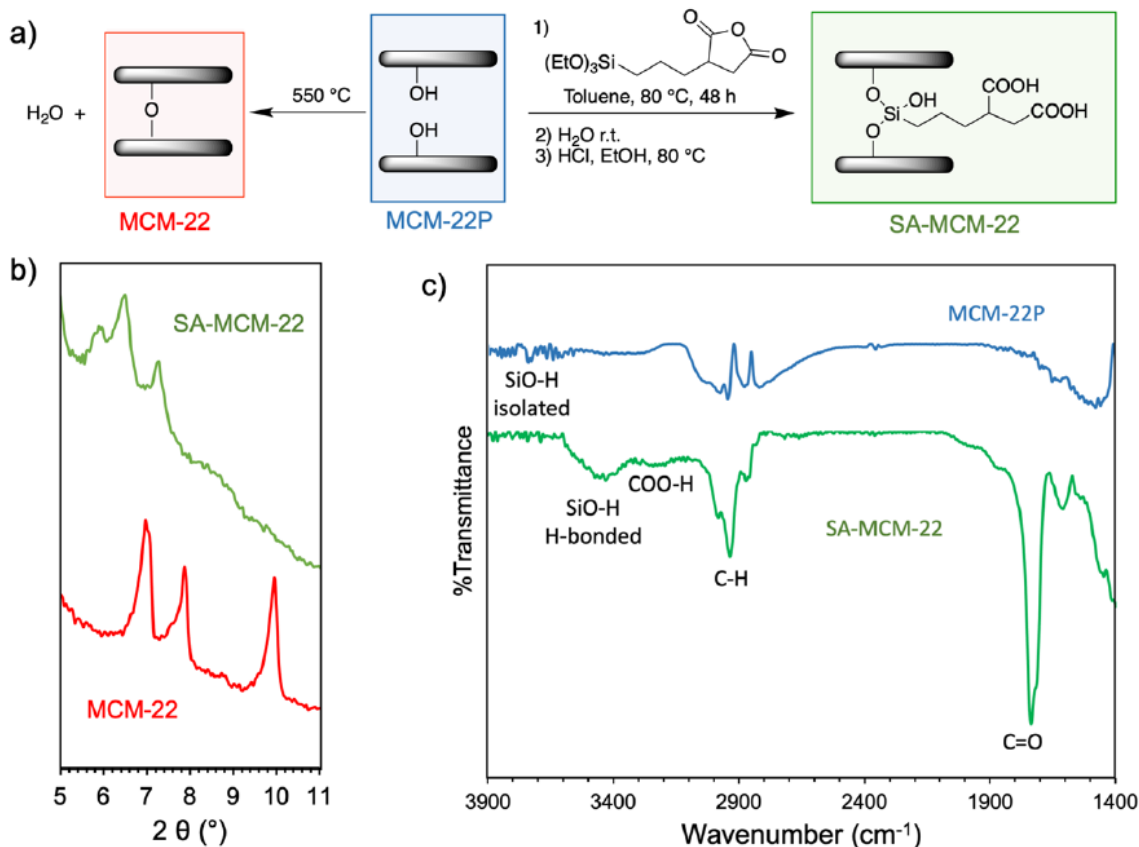
Fig. S4. (a) Synthesis of MCM-22 (red, left) and pillared SA-MCM-22 (green, right) from MCM-22P (blue, middle) by calcination and reaction with succinic acid triethoxysilane, respectively. (b) XRD patterns of the products show a shift of the low index planes in the pillared SA-MCM-22 to smaller angles than the calcined MCM-22 indicating larger d-spacing. (c) FTIR spectrum of the SA-MCM-22 confirms the presence of the pillaring group in the final compound.

### ESI6. Synthesis and XRD and FTIR analysis of pillared MCM-22

In **Fig. S4a**, we provide a schematic for the conversion on MCM-22P either to MCM-22 by calcination, or to AP-MCM-22 by pillaring. XRD data comparing MCM-22 and AP-MCM-22 is shown in **Fig, S4b**. Analysis via Fourier transform infrared (FTIR) spectroscopy (**Fig. S4c**) confirms the presence of the pillaring agent in the resulting material. Intense carbonyl peaks are observed at 1737 cm^{-1} along with C–H stretching bands from 2850 cm^{-1} to 2980 cm^{-1}. All these bands are absent in the precursor MCM-22P. Isolated silanols in the precursor were at 3731 cm^{-1} and no longer exist in the product. Additional features in the pillared SA-MCM-22 product include H-bonding silanols indicated by the broad band

centered at ca. 3430 cm^{-1} and a smaller broad band assigned to the carboxylic acid groups centered at ca. 3210 cm^{-1}.

ESI7. Analysis of interlayer spacings in MCM-22 and AP-MCM-22 from STEM

First, we briefly discuss specimen preparation for scanning transmission electron microscopy (STEM) imaging and image analysis. Roughly, 2 mL of dilute aqueous suspension containing as received MCM-22 and pillared MCM-22 type specimen, respectively, were placed on hydrophilized Quantifoil® (QF) holey carbon copper-supported grids and allowed to dry at room temperature. QF grids prepared in this manner were stored overnight in a desiccator before imaging. Imaging of interlayer spacings of zeolitic MCM-22 type materials was performed by using an aberration-corrected Thermo Scientific Titan Themis Cubed operating at 200 kV and hosted in the Sensitive Instrument Facility of Ames National Laboratory. Image processing was carried out using offline Gatan Microscopy Suite® software (GMS, Gatan Microscopy Suite® (GMS) software version 3.22.1461.0 - http://www.gatan.com/installation-instructions).
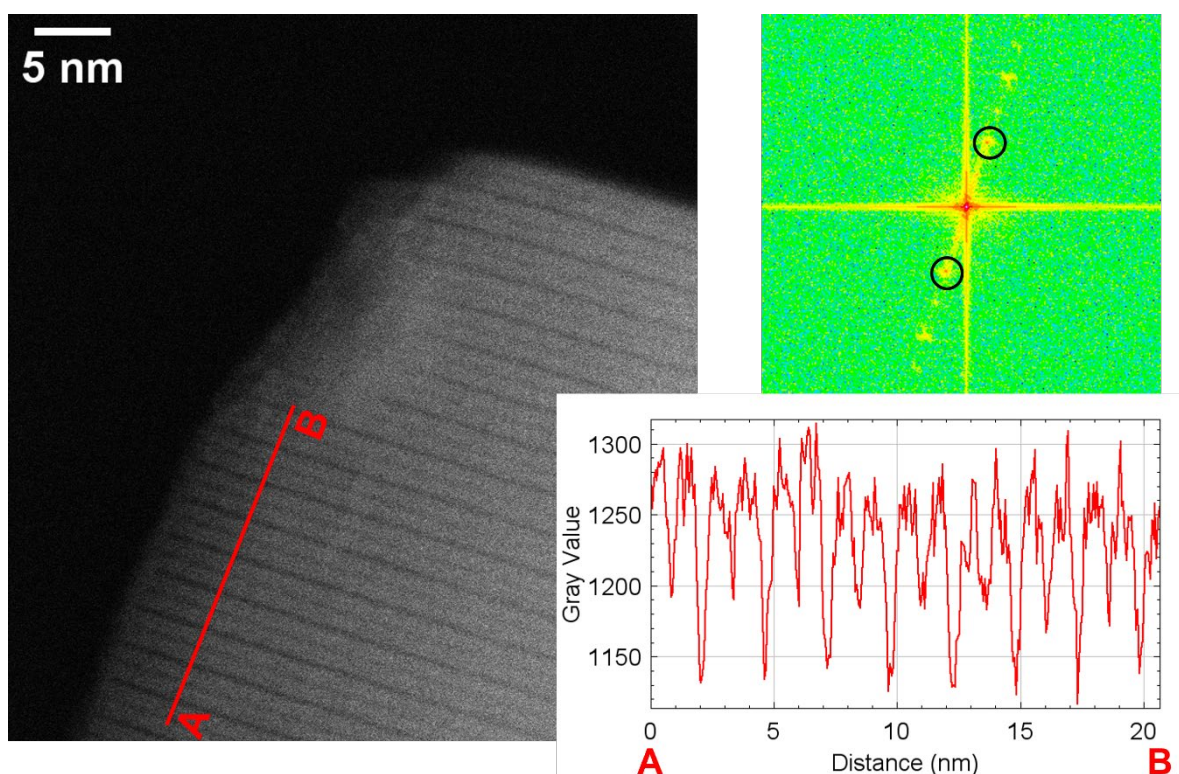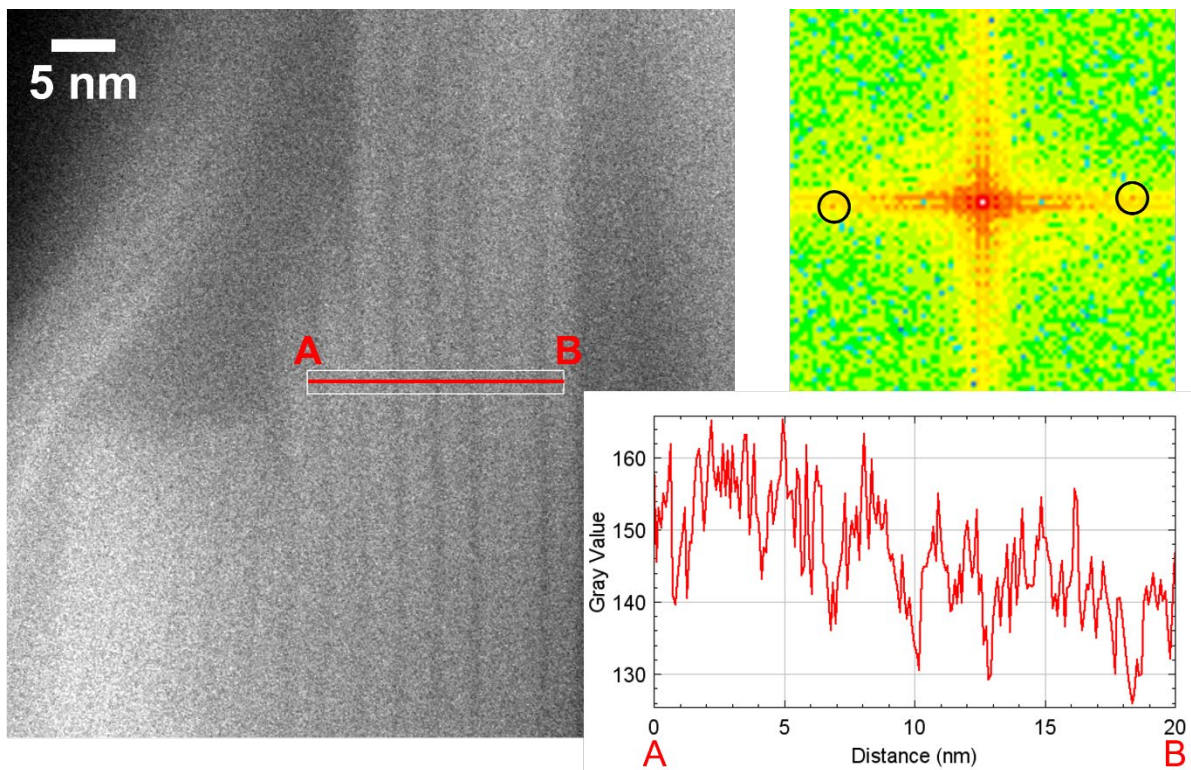

Fig. S5. MCM-22 sample of with Si:Al = 51:1. Left: A STEM image. Upper right: fast Fourier transform of the images where the spots associated with interlayer periodicity. Lower right: grayscale line scans orthogonal to the layers.

In **Fig. S5**, we show a STEM image of an MCM-22 sample with Si:Al = 51:1, including a grayscale line scan orthogonal to the layers. The darkest lines in the image are the grayscale minima, and are quite sharp, allowing direct estimate of the spacing between individual adjacent layers or periodicity. From the STEM image in **Fig. S5**, we obtain the

spacing values of about 25.8, 25.3, 24.7, 26.4, 27.7, 23.1, and 25.3 Å, quite narrowly distributed by about an average of 24.7 Å.

The STEM image becomes much noisier after exposure to the pillaring agent (succinic anhydride), as shown in **Fig. S6**. Nevertheless, the grayscale minima are still reasonably well resolved, and lead to the interlayer spacing estimates of about 33.0, 26.2, 33.0, and 27.2 Å with a significantly higher average and much broader distribution than **Fig. S5**.

Fig. S6. SA-MCM-22 sample of with Si:Al = 51:1 after exposure to the pillaring agent, succinic anhydride. Left: A STEM image. Upper right: fast Fourier transform of the images where the spots associated with interlayer periodicity. Lower right: grayscale line scans orthogonal to the layers.

ESI8. MD simulation parameters with empirical ReaxFF

In **Section 4**, MD simulations with an empirical ReaxFF [45, 46] using QuantumATK software [44] are utilized, prior to the final first principles DFT optimization for a given configuration. Based on the information from our preliminary studies, we always choose the NVT ensemble and the Nosé–Hoover thermostat for the MD procedure by implementing two simulation steps: first quenching and then annealing [58]. For the quenching, we set the temperature from 400 K to 300 K with a cooling rate of −5 K/ps and a simulation time of 20 ps. For the annealing, we set a temperature of 300 K and simulation time of 40 ps. The time step is always set to be 0.5 fs.

ESI9. Characterization of different classes of H-bonding

Table S5. Geometric and energetic parameters of the three basic types of H-bonds based on the Jeffrey's classification as suggested by Steiner [47]. $s_{H \cdots A}$, s_{X-H}, and s_{XA} are the corresponding atomic spacings between H and A, between X and H, and between X and A. $\phi_{X-H \cdots A}$ is the bond angle. A negative bond energy indicates the attraction, and its magnitude indicates the interaction strength.

	Type S	Type M	Type W
Interaction strength	Strong (S)	Moderate (M)	Weak (W)
Feature	covalent-like	electrostatic	vdW-like
$s_{H \cdots A}$	1.2 to 1.5 Å	1.5 to 2.2 Å	> 2.2 Å
s_{X-H} versus $s_{H \cdots A}$	$s_{X-H} \approx s_{H \cdots A}$	$s_{X-H} < s_{H \cdots A}$	$s_{X-H} \ll s_{H \cdots A}$
s_{XA}	2.2 to 2.5 Å	2.5 to 3.2 Å	> 3.2 Å
$\phi_{X-H \cdots A}$	170° to 180°	130° to 180°	90° to 180°
Bond energy	−1.73 to −0.65 eV	−0.65 to −0.17 eV	> −0.17 eV

ESI10. Atomic spacings between H atoms and their surrounding atoms

To find the H-bonds as well as compare with the geometry of trimethylsilanol molecule, in **Table S6** we list all atomic spacings, s, between H atoms and their surrounding atoms in various configurations. Relative to the geometric parameters of a trimethylsilanol molecule, the s values of other configurations have no noticeable changes, e.g., any covalent O-H bond length in a hydroxyl group OH is about 0.97 Å, any covalent C-H bond length in a methyl group CH_3 is about 1.10 Å, any H-Si distance in a SiOH group are about 2.30 Å, and any H-H distance in a methyl group CH_3 is about 1.78 Å, as listed in **Table S6**. Also, any H-H distance in a pair of (upper and lower) hydroxyl groups of the precursor configuration (**Fig. 1d**) is about 2.14 Å, while the H-H distance in a pair of (upper and lower) hydroxyl groups of the 50% −OH + 50% (−O_2)SiOHCH_3 configuration (**Fig. 4c**) is about 2.03 Å (see **Table S6**).

As revealed by **Fig. 5c**, the acceptor O7 in the H-bond O155−H247···O7 is an O atom of a Si-O-Si bridge at the upper layer surface, while the donor O155−H247 is a hydroxyl group OH in O_ISi(OH)$_2$$CH_3$ connecting the lower layer. Thus, O155−H247···O7 binds the upper and lower layers. Similarly, the acceptor O10 in the H-bond O154−H254···O10 is an O atom of a Si-O-Si bridge at the lower layer surface, while the donor O154−H254 is a hydroxyl group OH in O_{IV}Si(OH)$_2$$CH_3$ connecting the upper layer. Thus, O154−H254···O10 also binds the upper and lower layers. The significantly stronger H-bonding between the upper and lower layers facilitates shrinkage of the interlayer space, relative to the significantly weaker bonding only from vdW or vdW-like interactions.

Table S6. Atomic spacings *s* between H atoms and their surrounding atoms from our optB88-vdW calculations. Only the atomic spacings less than 2.3 Å are listed. The four atomic spacings with bold fonts indicate the H-bonds in **Fig. 5c**.

Precursor [a]	*s* (Å)	50% A1 [b]	*s* (Å)	100% A1 [c]	*s* (Å)	100% A2 [d]	*s* (Å)	TMS [e]	*s* (Å)
H219-O2	2.278	H225-O148	0.969	H228-O149	0.969	**H247-O7**	**1.953**	H15-O4	0.968
H219-O146	0.971	H226-O3	2.167	H232-O150	0.969	H247-O155	0.976		
H220-O2	0.971	H226-O147	0.972			**H248-O151**	**1.784**		
H220-O146	2.267	H227-O3	0.972			H248-O156	0.986		
H221-O1	2.288	H227-O147	2.125			H249-O157	0.971		
H221-O145	0.971					H250-O158	0.973		
H222-O1	0.971					H251-O151	0.973		
H222-O145	2.259					H252-O152	0.971		
						H253-O153	0.986		
						H253-O158	**1.784**		
						H254-O10	**1.952**		
						H254-O154	0.976		
		H222-C1 [f]	1.098	H225-C1	1.097	H235-C1	1.099	H6-C1	1.098
		H223-C1	1.098	H226-C1	1.098	H236-C2	1.098	H7-C1	1.099
		H224-C1	1.097	H227-C1	1.097	H237-C3	1.098	H8-C1	1.099
				H229-C2	1.098	H238-C4	1.100	H9-C2	1.098
				H230-C2	1.098	H239-C1	1.096	H10-C2	1.098
				H231-C2	1.099	H240-C2	1.099	H11-C2	1.098
						H241-C3	1.099	H12-C3	1.098
						H242-C4	1.099	H13-C3	1.099
						H243-C1	1.100	H14-C3	1.099
						H244-C2	1.096		
						H245-C3	1.096		
						H246-C4	1.096		
H219-Si148	2.280	H225-Si221	2.289	H228-Si223	2.292	H249-Si233	2.293	H15-Si5	2.299
H220-Si149	2.281	H226-Si150	2.275	H232-Si224	2.287	H252-Si232	2.293		
H221-Si150	2.278	H227-Si151	2.282						
H222-Si147	2.284								
H219-H220	2.139	H222-H223	1.779	H225-H226	1.779	H235-H239	1.778	H6-H7	1.775
H221-H222	2.143	H222-H224	1.779	H225-H227	1.779	H235-H243	1.784	H6-H8	1.774
		H223-H224	1.778	H226-H227	1.779	H236-H240	1.780	H7-H8	1.771
		H226-H227	2.029	H229-H230	1.780	H236-H244	1.778	H9-H10	1.776
				H229-H231	1.776	H237-H241	1.780	H9-H11	1.776
				H230-H231	1.780	H237-H245	1.778	H10-H11	1.774
						H238-H242	1.784	H12-H13	1.775
						H238-H246	1.781	H12-H14	1.775
						H239-H243	1.781	H13-H14	1.771
						H240-H244	1.781		
						H241-H245	1.781		
						H242-H246	1.778		

[a] "Precursor" denotes the "100% OH" supercell with 222 atoms (**Fig. 1d**).

[b] "50% A1" denotes the "50% OH + 50% (−O$_2$)SiOHCH$_3$" supercell with 227 atoms (**Fig. 4c**).

[c] "100% A1" denotes the "0% OH + 100% (−O$_2$)SiOHCH$_3$" supercell with 232 atoms (**Fig. 4d**).

[d] "100% A2" denotes the "0% OH + 100% (−O)Si(OH)$_2$CH$_3$" supercell with 254 atoms (**Fig. 5b** or **5c**).

[e] "TMS" denotes a trimethylsilanol molecule with 15 atoms (left of **Fig. 4a** or **5a**).

[f] As an example, "H222-C1" in the third column denotes the atomic spacing between the H atom with ID number 222 (i.e., the 222th atom H) and the C atom with ID number 1 (i.e., the 1st atom C) in the "50% OH + 50% (−O$_2$)SiOHCH$_3$" supercell (**Fig. 4c**) with 227 atoms corresponding to 227 ID numbers. The analogous statement applies to each of other atomic pairs in this table.

Let us also examine two rest H-bonds. From **Fig. 5c**, H248 in O156−H248···O151 is a H atom of a hydroxyl group OH in O$_{II}$Si(OH)$_2$CH$_3$, while the donor atom O156 and the

acceptor atom O151 are from the hydroxyl groups in $O_{II}Si(OH)_2CH_3$ and $O_ISi(OH)_2CH_3$, respectively. Both $O_{II}Si(OH)_2CH_3$ and $O_ISi(OH)_2CH_3$ only connect the lower layer. Then, the H-bond of O156−H248···O151 does not contribute to the interlayer spacing reduction. From the similar analysis, neither does the H-bond of O153−H253···O158.

ESI11. Relative thermodynamic stability of pillared versus grafted configurations

To assess the relative thermodynamic stability of pillared versus grafted materials based on DFT analysis of energies, one can start with the same "reactant" system on the left, as illustrated in **Fig. S7**. Then, one just compares the energies of the two distinct pillared versus grafted "product" systems on right. In evaluating the energy difference of two "product" systems, note that the 8 RH cancel out, so that the result does not depend on the choice of R or the corresponding energy E_{RH}. In our DFT analysis, R = CH_3. The energy difference between pillared and grafted configurations can be calculated as

$$\Delta E = E(\text{grafted system}) - E(\text{pillared system}) = E_{\text{graft}} + E_{\text{precursor}} - 2E_{\text{pillar}} - 4E_{H_2O},$$

where E_{H_2O} is the energy of an isolated H_2O molecule; $E_{\text{precursor}}$, E_{pillar}, and E_{graft} are the energies of precursor, pillared, and grafted unit cells, respectively. Using the values of these energies from our DFT calculations, we obtain $\Delta E = -1.013$ eV, indicating that the grafted configuration is thermodynamically favored.
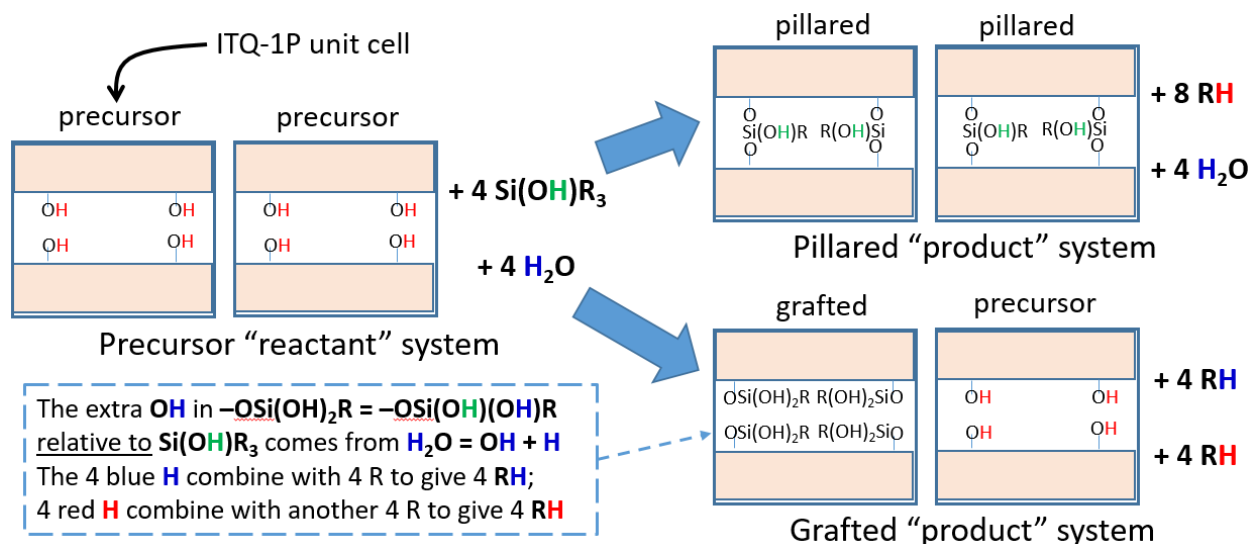
 Fig. S7. Illustration for computational setup for determination of the relative thermodynamic preference of pillared versus grafted configurations.

References

For Refs. [1–48], see the main text.

[49] F. D. Stacey, B. J. Brennan and R. D. Irvine, *Geophys. Surveys*, 1981, **4**, 189–232.

[50] P. Vinet, J. R. Smith, J. Ferrante and J. H. Rose, *Phys. Rev. B*, 1987, **35**, 1945–1953.

[51] Y. Jiang, Y. Shi, X. Xiang, J. Qi, Y. Han, Z. Liao and T. Lu, *Phys. Rev. Appl.*, 2019, **11**, 054088.

[52] L. Levien, C. T. Prewitt and D. J. Weidner, *Am. Miner.*, 1980, **65**, 920–930.

[53] G. A. Lager, J. D. Jorgensen and F. J. Rotella, *J. Appl. Phys.*, 1982, **53**, 6751–6756.

[54] R. M. Hazen, L. W. Finger, R. J. Hemley and H. K. Mao, *Solid State Commun.*, 1989, **72**, 507–511.

[55] H. J. McSkimin, P. Andreatch and R. N. Thurston, *J. Appl. Phys.*, 1965, **36**, 1624–1632.

[56] G. Hautier, S. P. Ong, A. Jain, C. J. Moore and G. Ceder, *Phys. Rev. B*, 2012, **85**, 155208.

[57] V. V. Narkhede and H. Gies, *Chem. Mater.*, 2009, **21**, 4339–4346.

[58] Y. Han, I. I. Slowing and J. W. Evans, *J. Chem. Phys.*, 2020, **153**, 124708.